Supplementary Information (SI) for Energy & Environmental Science.

Persistent photothermal CO_2 methanation without external energy input

Experimental Section

1.1 Chemicals for catalysts

Commercial nickel nitrate hexahydrate (Ni $(NO_3)_2 \cdot 6H_2O$) is purchased from Kermel Co., LTD. The citric acid ($C_6H_8O_7 \cdot H_2O$) is purchased from Tianjin Bohuatong Chemical Products Sales Co., LTD. Cerium nitrate (Ce $(NO_3)_3 \cdot 6H_2O$, AR) is purchased from Tianjin Kemel Chemical Reagent Co., LTD. Nitric acid (HNO_3, AR), aqueous ammonia (NH_4OH, 25 wt%, AR), and ethylenediamine ($C_2H_8N_2$, AR) are purchased from Damao Chemical Reagents Factory. All chemicals are used directly without further treatment. TiC and Cu powders are purchased from ZhongNuo Advanced Material (Beijing) Technology Co. Ltd. The purity of TiC and Cu is 99.99%.

1.2 Catalysts preparation

2D $Ni_1Ce_1O_3$

Firstly, 5g citric acid, 2g $Ce(NO_3)_3 \cdot 6H_2O$ and 0.339g $Ni(NO_3)_2 \cdot 6H_2O$ are added into the beaker. Secondly, 2.5 mL HNO_3 and 6 mL aqueous ammonia are added into the mixture to stir as homogeneous solution. Thirdly, the solution is stirred at 80 °C for 8 hours to form a gel. Fourthly, the gel is put into an oven at 100 °C for 24 hours to remove additional water. Fifthly, the dried gel is loaded into a muffle furnace with 300 °C of temperature. The gel would explode and burned rapidly to form 2D $Ni_1Ce_1O_3$. The yield of 2D $Ni_1Ce_1O_3$ is ~1 g. Attention, during the preparation process, a large amount of NO_x gas will be generated and we need to wear a gas mask during the operation process.

Ni/CeO_2

Firstly, 2g $Ce(NO_3)_3 \cdot 6H_2O$ and 1.339g $Ni(NO_3)_2 \cdot 6H_2O$ are dissolved into 10 mL of deionized water to form a homogeneous solution. Secondly, 1 mL aqueous ammonia is dropped into the solution with successive stirring and the precipitation is separated from solution. Thirdly, the precipitation is calcined in a muffle furnace at 450 °C for 5 hours with a heating rate of 1 °C min^{-1}. Fourthly, the annealed sample is reduced by 10% H_2/Ar at 400 °C for 6 hours with a heating rate of 1 °C min^{-1}, thus achieving Ni/CeO_2. Attention, during the preparation process, a large amount of NO_x gas will be generated and we need to wear a gas mask during the operation process.

2D CuO-CeO_2

$Cu(NO_3)_2$ and polyvinyl pyrrolidone are purchased from Macklin Co., Ltd, urea and $Ce(NO_3)_3 \cdot 6H_2O$ are purchased from Kemel chemical industry Co., Ltd. All chemicals, including ethanol (BeiLian chemical industry Co., Ltd), are used without further treatment.

Typically, 3.252 g $Cu(NO_3)_2$,18.99g $Ce(NO_3)_3 \cdot 6H_2O$ and 26.26 g of citric acid are dissolved in 50 ml of ethanol mixed with 7.5 ml H_2O. After stirring for 2 hours, then 22.5 ml propylene oxide is added into the above solution dropwise. Finally, the recovered product is calcined at 450 °C for 6h and 550 °C for 4 h to remove organic residues. The obtained materials are denoted as 2D CuO-CeO_2.

1.3 Characterizations

The TEM images are obtained on a JEOL2100plus transmission electron microscope operating at 200 kV. The samples are prepared by dropping water/ethanol dispersion of samples onto ultrathin carbon film and immediately evaporating the solvent. The aberration-corrected high-angle annular dark-field scanning TEM (AC-HAADF-STEM) images and STEM-EDX elemental mapping are collected on a JEM-ARM200F transmission electron microscopy working at 200 kV, equipped with a probe spherical aberration corrector. The SEM images are acquired from FEI Nova Nano SEM450 scanning electron microscopes. XRD measurements of the obtained catalyst powders are performed on a Rigaku MiniFlex 600 diffractometer with a Cu-Kα X-ray radiation source ($\lambda = 0.154056$ nm). Typically, 2 mg of powders are placed on an amorphous silica substrate and the XRD patterns are record at a scan rate of 2° min^{-1}. XPS measurements are performed by a Thermo VG ESCALAB-250 system with Al-Kα and Mg-Kα source operated at 15 kV. The binding energies are referred to the C 1s peak (284.8 eV) from adventitious carbon. Infrared (IR) photograph is taken with a camera (Fluke Ti300, America). The IR radiation and IR emissivity of samples are tested by integrating sphere-equipped FTIR with a heater substrate (HYPERION 3000, Bruker Optics). Zennium_Pro (Zahner, Germany) is an electrochemical workstation. N_2 sorption isotherms are measured at 77 K on a BELSORP MAX G absorption apparatus. Before tests, the samples are pre-activated at 120 °C for 12 h. The pore size distributions were estimated by the DFT method from a N_2 sorption experiment at 77 K. The metal content in our catalysts is determined by an ICP-OES spectrometer (Model Optima 2000, PerkinElmer). A series of solutions for the measurements are prepared by dissolving 20 mg of samples in 4 mL of aqua regia (75 vol.% HCl and 25 vol.% HNO_3). The solution is left overnight to allow complete dissolution. The resultant solution is diluted to 50 mL with deionized water in a volumetric flask and then analyzed using ICP-OES. The ultraviolet-visible-infrared absorption spectrum (UV-vis-IR) and IR emission were tested by Hitachi Limited U4100 (Japan) and FTIR spectrometer (Bruker, VERTEX 70 FT-IR). The light intensity is measured by optical power meter (PM100D+S425C, THORLABS). CO_2-TPD is carried out in a quartz tube. 0.05 g of catalyst is treated in Ar gas at 300 °C for 4 hours. After cooling to ambient temperature, CO_2 is adsorbed for 4 hours to saturation, and the Ar gas is blown for 30 minutes at room temperature before programmed temperature rise desorption. The heating rate was 2 °C min^{-1}, and the desorbed CO_2 is detected by gas chromatography (GC) 7890A equipped with a TCD detector.

The Ni K-edge, Ce L-edge X-ray fine absorption structure data were collected on the beamline at Shanghai Synchrotron Radiation Facility (SSRF). All samples mixed with BN are coating on 3 M tape. A Si (111) crystal monochromator was used to filter the incident beam. We used IFEFFIT software to calibrate the energy scale, correct the background signal and normalize the intensity. In this work, the transmission mode was used to detect the Extended X-ray absorption fine structure of Ni K-edge and Ce L-edge. The spectra are normalized concerning the edge height after subtracting the pre- (-150 eV to -30 eV) and post-edge (50 eV to 800 eV) backgrounds using Athena software.[1] To extract the EXAFS oscillations, the background was removed in k-space using a five-domain cubic spline.

1.4 First principle calculations

We have employed the Vienna Ab Initio Package (VASP)[2, 3] to perform all the density functional theory (DFT) calculations within the generalized gradient approximation (GGA) using the PBE formulation.[4] We have chosen the projected augmented wave (PAW) potentials[5, 6] to describe the ionic cores and take valence electrons into account using a plane wave basis set with a kinetic energy cutoff of 450 eV. Partial occupancies of the Kohn−Sham orbitals were allowed using the Gaussian smearing method and a width of 0.05 eV. The on-site corrections (DFT+U) has been applied to the 4f electron of Ce atoms (U_{eff}=4.5 eV) by the approach from Dudarev et al.[7] The electronic energy was considered self-consistent when the energy change was smaller than 10^{-5} eV. A geometry optimization was considered convergent when the force change was smaller than 0.02 eV/Å. Grimme's DFT-D3 methodology was used to describe the dispersion interactions.[8]

The equilibrium lattice constant of cubic CeO_2 unit cell was optimized, when using a 11×11×11 Monkhorst-Pack k-point grid for Brillouin zone sampling, to be a=5.479 Å. We then use it to construct a $CeO_2(111)$ surface model with $p(4\times4)$ periodicity in the X and Y directions and 3 stoichiometric layers in the Z direction by vacuum depth of 15 Å in order to separate the surface slab from its periodic duplicates. This model comprises of 48 Ce and 96 O atoms. Model 1 was built by adding one Ni_{10} cluster onto the $CeO_2(111)$ surface. Model 2 was built by replacing half of Ce atoms with Ni atoms. During structural optimizations, the Γ point in the Brillouin zone was used for k-point sampling, and the bottom two stoichiometric layers were fixed while the rest were allowed to fully relax.

The adsorption energy (E_{ads}) of adsorbate A was defined as

$$E_{ads} = E_{A/surf} - E_{surf} - E_{A(g)} \qquad (1)$$

where $E_{A/surf}$, E_{surf} and $E_{A(g)}$ are the energy of adsorbate A adsorbed on the polyimide, the energy of clean polyimide, and the energy of isolated A molecule in a cubic periodic box with a side length of 20 Å and a 1×1×1 Monkhorst-Pack k-point grid for Brillouin zone sampling, respectively.

1.5 Thermal catalytic test

The thermocatalytic activity of catalysts for CO_2 hydrogenation is tested by the fixed-bed reactor (XM190708-007, DALIAN ZHONGJIARUILIN LIQUID TECHNOLOGY CO., LTD) in continuous flow form. Typically, 2 mg of catalysts were loaded in a quartz tube for thermocatalytic CO_2 methanation test, the flow of feed gas was the mixture of 3 mL min^{-1} of CO_2 and 12 mL min^{-1} of H_2. The reaction products were tested by gas chromatography (GC) 7890A equipped with FID and TCD detectors. In this regard, the volume of 1 mol gas is considered to be 24.5 L.

1.6 The preparation of TiC/Cu based device

The based reaction tube is a stainless tube. Then, the SP-0707AS magnetron sputtering is used to deposit Cu film and TiC film, which has a 4-axis rotation system to rotate bases. Cu and TiC are used as targets; the working gas is Ar with 99.99 % purity. Before the deposition process, the stainless is washed orderly with deionized water, acetone and ethanol. The deposition of Cu substrate and TiC film on reaction tube is first using glow-discharge to clean stainless tube, then depositing Cu layer by Cu target and TiC film by TiC target orderly, finally taking out the sample after passive cooling. Specific parameters: the power is 5 KW, the sputtering pressure is 9×10^{-2} Pa, the bias voltage is 150 V, the sputtering temperature is 70 °C, the sputtering time for Cu layer, TiC film is 25 min, 3 min, respectively. The followed glass vacuum layer has 1×10^{-3} Pa of pressure.

1.7 Photothermal CO_2 methanation test

10 mg of 2D $Ni_1Ce_1O_3$ was loaded in TiC/Cu based device and irradiated by light source (DL3000), the flow of feed gas was the mixture of 15 mL min^{-1} of CO_2 and 60 mL min^{-1} of H_2.

The reaction products were tested by gas chromatography (GC) 7890A equipped with FID and TCD detectors. In this regard, the volume of 1 mol gas is considered to be 24.5 L.

Laboratory self-operating photothermal CO_2 methanation test

The laboratory self-operating photothermal CO_2 methanation is tested by the TiC/Cu based device in continuous flow form with a feed gas containing 24 L h^{-1} of CO_2 and 96 L h^{-1} of H_2. Typically, 10 g of 2D $Ni_1Ce_1O_3$ is placed in the TiC/Cu based device irradiated by light source (DL3000) with 0.7 kW m^{-2} of intensity. After 3 hours irradiation, the light source is cut off and the feed gas is still provided with constant flow rate of 120 L h^{-1}. In this regard, the volume of 1 mol gas is considered to be 24.5 L.

Enthalpy change energy of chemicals

The enthalpy change energy of CO_2 (g), CH_4 (g), H_2 (g), H_2O (g) is -393.505, -74.852, 0, -241.818 kJ mol^{-1}, respectively.

The (g) indicated the gas state.

Calculation of heat input power of self-operating methanation test

The heat input power (F) is calculated as follows:

$$F= (\Delta H*\tau)/(S*3600) \qquad (2)$$

ΔH is the reaction Enthalpy change energy ($CO_2 (g) + 4H_2 (g) \rightarrow CH_4 (g) + 2H_2O (g)$, $\Delta H= -164.98$ kJ mol^{-1}), τ (mol) is the CH_4 generation amount per hour, S is the surface area of devices. All the devices are in tube form with 1.6 cm of diameter and 40 cm of length. Thus, the $S=0.016 m*0.4 m*3.14=0.0201 m^2$. After calculation, the F is 1.95, 1.88 kW m^{-2} at 0.86, 0.83 mol h^{-1} of CH_4 generation rates, respectively.

Calculation of heat output power of self-operating methanation test

The power of heating feed gas (P) to 340 °C is calculated as follows:

$$P= (\theta*\Delta*\lambda/24.5)/(S*3600) \qquad (3)$$

θ (0.03 KJ mol^{-1} K^{-1}) is the average isobaric heat capacity of the feed gas mixed with CO_2 and H_2 (the data of isobaric heat capacity were referred from Lange's Handbook). Δ is the temperature difference (315 K=340 °C-25 °C). λ is the total gas flow rate of 120 L h^{-1}. S is the surface area of devices. All the devices are in tube form with 1.6 cm of diameter and 40 cm of length. Thus, the S=0.016 m*0.4 m*3.14=0.0201 m^2. After calculation, the P was 0.64 kW m^{-2} at 340 °C.

At 340 °C, the heat input power (F) is equal to the heat output power.

Therefore, the system heat dissipation (Q) = F-P = 1.24 kW m^{-2}.

1.8 Outdoor self-operating photothermal methanation reaction test

The amplified TiC/Cu based device was used in outdoor self-operating CO_2 hydrogenation. 2 kg of 2D $Ni_1Ce_1O_3$ was loaded in TiC/Cu based device with 6 m length and 5 cm diameter. The flow rate of feed gas was 50 m^3 h^{-1} containing 10 m^3 h^{-1} of CO_2 and 40 m^3 h^{-1} of H_2. The installation of parabolic reflector (6 m length and 0.8 m width) was based on the ecliptic plane to make sunlight focus on the TiC/Cu based device. The water-cooling system was used to maintain 300 °C temperature of catalysts. The flow of the produced gas was counted by the vortex flowmeter, and we used (GC) 7890A equipped with FID and TCD detectors to analyze the content of CH_4 in produced gas.

1.9 Self-operating photothermal toluene oxidation test

In this experiment, 10 g of 2D CuO-CeO_2 is placed at the middle of the TiC/Cu device, which is irradiated by a light source (DL-3000), and the flow of feed air is 240 L h^{-1} containing 5000 ppm of toluene. Then, the composition of the outlet gas is analyzed by an online gas chromatograph (GC) 7890A equipped with FID and TCD detectors.

Table S1. EXAFS fitting parameters of Ni in NiO, 2D $Ni_1Ce_1O_3$.

sample	Path	CN	$\sigma^2(10^{-3}$ Å$^2)$	R(Å)	ΔE_0(eV)
NiO	Ni-O	5.3±0.2	3.4±0.6	1.98±0.03	-3.3
2D $Ni_1Ce_1O_3$	Ni-O	6.0±0.3	3.7±0.8	2.27±0.02	5.2

Table S2. EXAFS fitting parameters of Ce in CeO_2, 2D $Ni_1Ce_1O_3$.

sample	Path	CN	$\sigma^2(10^{-3}$ Å$^2)$	R(Å)	ΔE_0(eV)
CeO_2	Ce-O	7.8±0.3	4.3±0.7	2.31±0.02	5.4
2D $Ni_1Ce_1O_3$	Ce-O	6.2±0.7	4.7±0.5	2.31±0.02	2.9

Table S3. The CO_2 methanation performance of 2D $Ni_1Ce_1O_3$ in comparison with the advanced CO_2 methanation catalysts under atmospheric pressure.

Catalysts	Temperature (°C)	CH_4 rate ($mmol\cdot g^{-1}\cdot h^{-1}$)	CH_4 Selectivity (%)	Refs.
2D $Ni_1Ce_1O_3$	**300**	**2138**	**99.5**	**This work**
Ru-Co/C	300	470.76	75.8	9
Ni@C-600	300	297.32	100	10
$RuCeO_x$	300	232	99	11
Ru/CeO_2	300	226.93	99	12
Ni/CeO_2-La	300	214.81	99.8	13
NiCeY	300	136.8	98	14
NiRuAl	300	124.27	99.5	15
Ru/TiO_2	300	90	100	16
Ru/Al_2O_3	300	75	100	17
Ru/TiO_2 (001)	300	19	100	18
Ru/r-TiO_2	277	55	98	19
Ru/CeO_2	270	147	100	20
2D $Ni_1Ce_1O_3$	**250**	**1000**	**99.5**	**This work**
Ni/CeO_2-SGM	250	63.84	95	21
MnNiZrRuCe	250	51	100	22
Ru/R-TiO_2	250	36.7	100	23
Ni/CeZr	250	19	100	24
Ru SA	250	14.7	95	25
$Ru/CeO_2/Al_2O_3$	250	12	100	26
Ru/CNT	250	11	100	27
Ru/MoO_3	250	1.6	100	28
MnNiZrRuCe	230	31	100	22
Ni/BN	230	16.2	100	29
1.5%Ru/Ni	214	123	100	30
2D $Ni_1Ce_1O_3$	**200**	**80.4**	**100**	**This work**
Ru/H_xMoO_{3-y}	200	16.1	100	31
fct-PdFe	200	10.6	100	32
Rh/Al nanoantenna	200	5	80	33

Table S4. Photothermal CO_2 methanation rate of reported state of the art of catalysts.

Catalysts	Light	External support	CH_4 rate ($mmol \cdot g^{-1} \cdot h^{-1}$)	Refs.
2D $Ni_1Ce_1O_3$	**1 sun**	**None**	**2901**	**This work**
2D $Ni_1Ce_1O_3$	**0.5 sun**	**None**	**773**	**This work**
Rh/Al nanoantenna	113 suns	200 ºC	550	[33]
Ni@C-600	43 suns	0.5 Mpa	488	[10]
NiAl-LDH	26.3 suns	None	278.8	[34]
Ru-Al_2O_{3-x}-L	22.7 suns	None	203.7	[35]
Ni@p-SiO_2-30	28 suns	None	200.4	[36]
Ni/$BaTiO_3$	29.3 suns	0.5 Mpa	103.7	[37]
SA Ni/Y_2O_3	1 sun	None	56.3	[38]
Ni/SiO_2-Al_2O_3	1 sun	150 ºC	54.5	[39]
Ni/TiO_2	12.3 suns	None	21.7	[40]
Ru/H_xMoO_{3-y}	7.5 suns	140 ºC	20.8	[31]

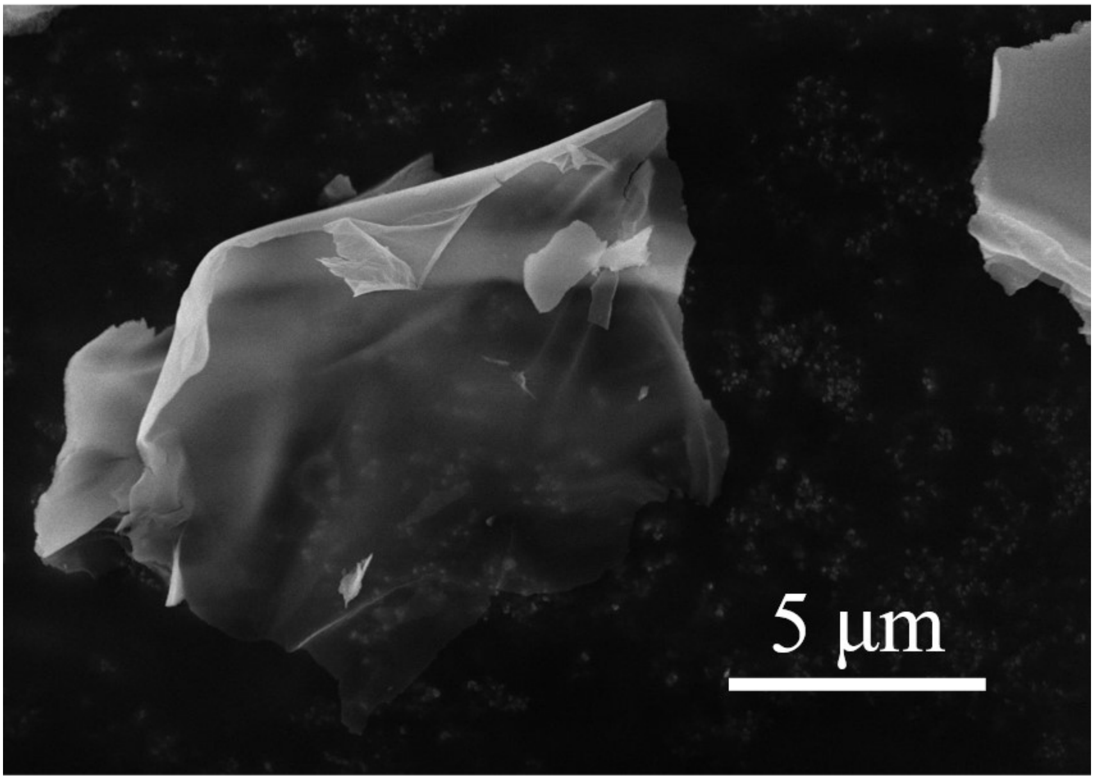

Fig. S1 SEM image of 2D $Ni_1Ce_1O_3$.

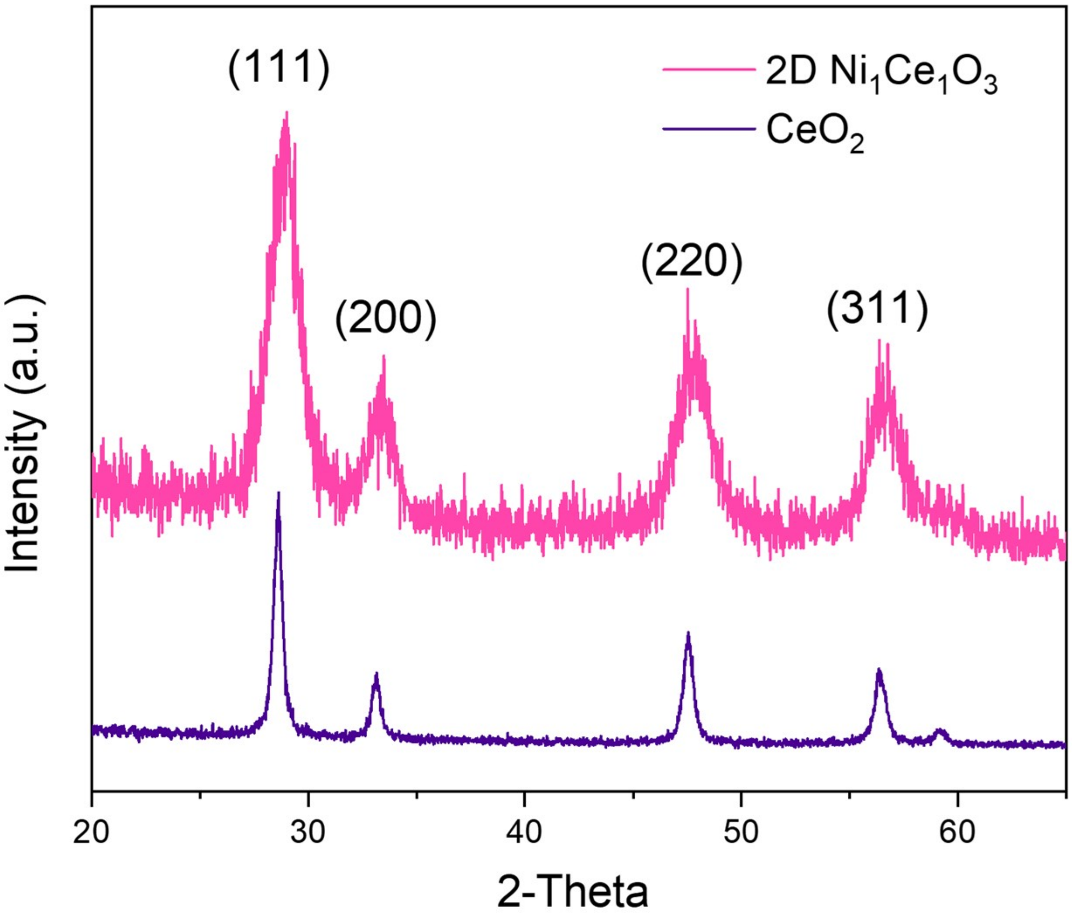

Fig. S2 XRD pattern of 2D $Ni_1Ce_1O_3$ and CeO_2.

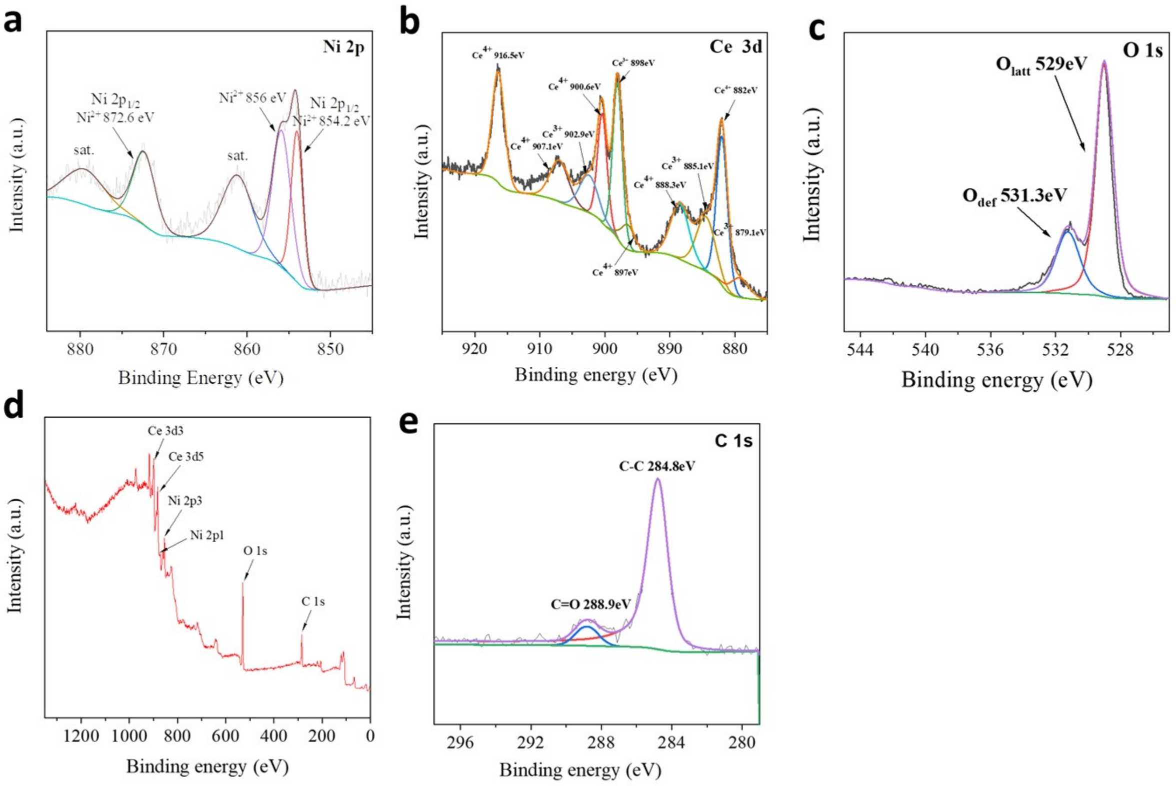

Fig. S3 The Ni 2p spectrum (a), Ce 3d spectrum (b), O 1s spectrum (c), survey (d), C 1s spectrum (e) of 2D $Ni_1Ce_1O_3$.

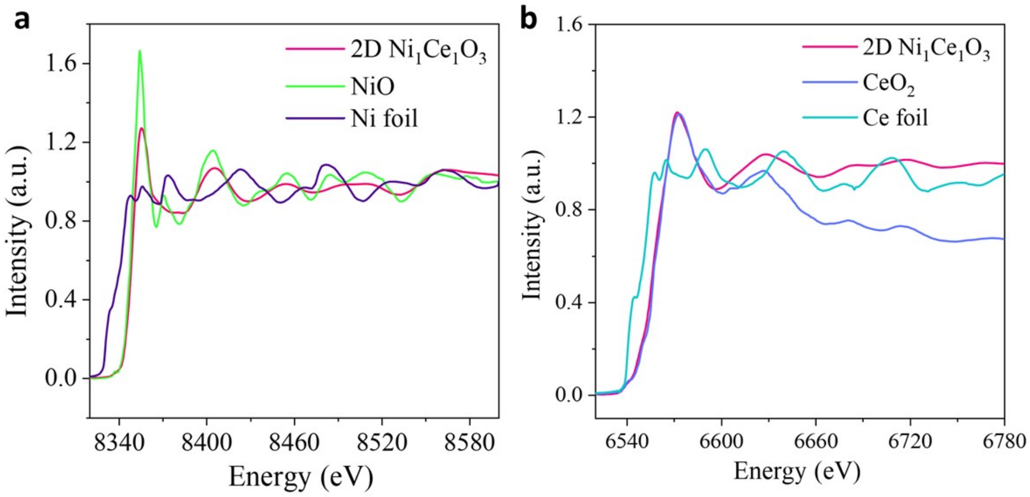

Fig. S4 (a) The Ni K-edge EXAFS of 2D $Ni_1Ce_1O_3$ with references of NiO and Ni foil. (b) The Ce L-edge EXAFS of 2D $Ni_1Ce_1O_3$ with references of CeO_2 and Ce foil.

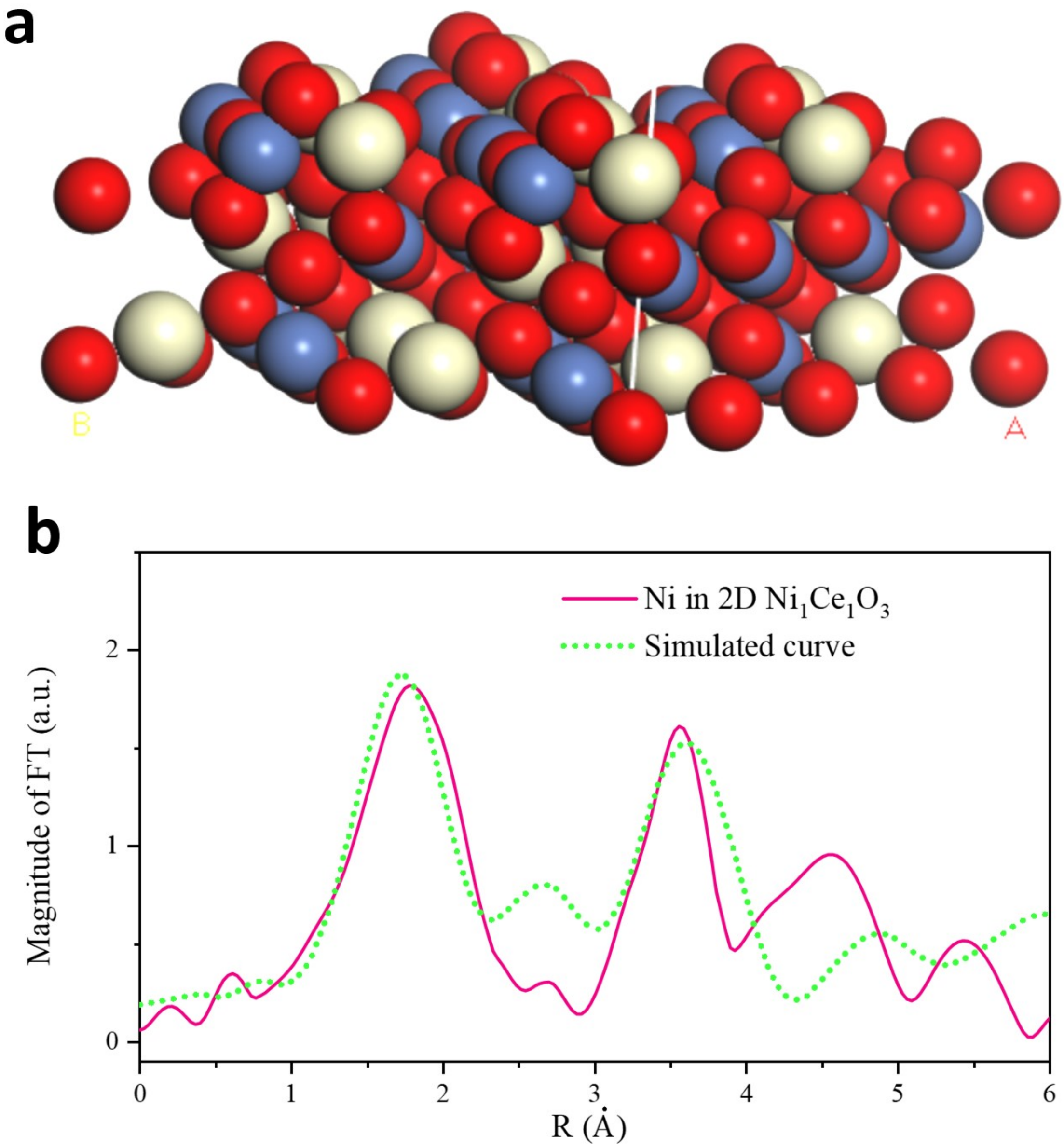

Fig. S5 (a) Atomic structure of the 2D $Ni_1Ce_1O_3$. (b) The simulated FTEXAFS curve of the proposed 2D $Ni_1Ce_1O_3$ structure (green line) and the measured 2D $Ni_1Ce_1O_3$ (purple line).

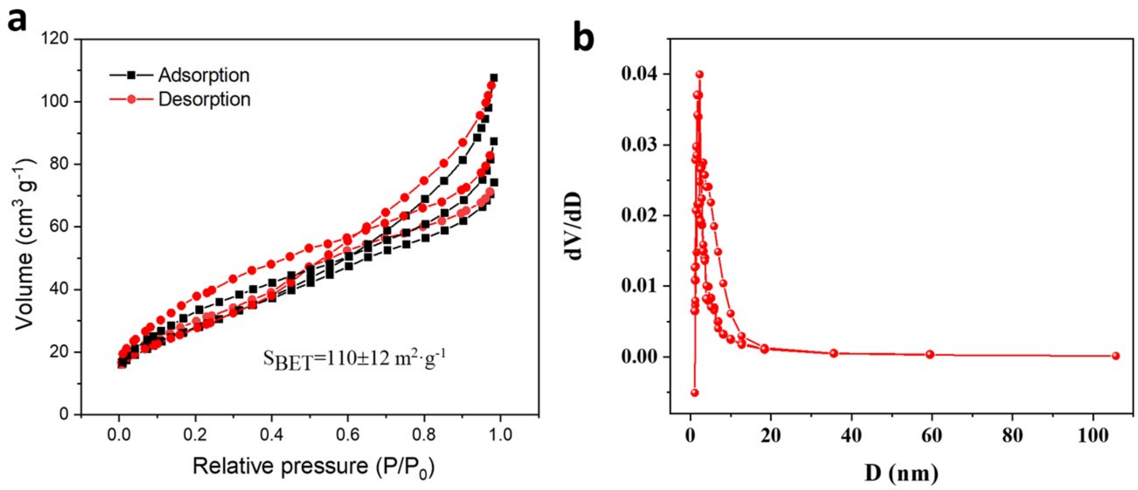

Fig. S6 (a) The nitrogen adsorption and desorption isotherms of 2D $Ni_1Ce_1O_3$. (b) Pore volume distribution curves of subsamples from the N_2 adsorption isotherm, using the BJH model.

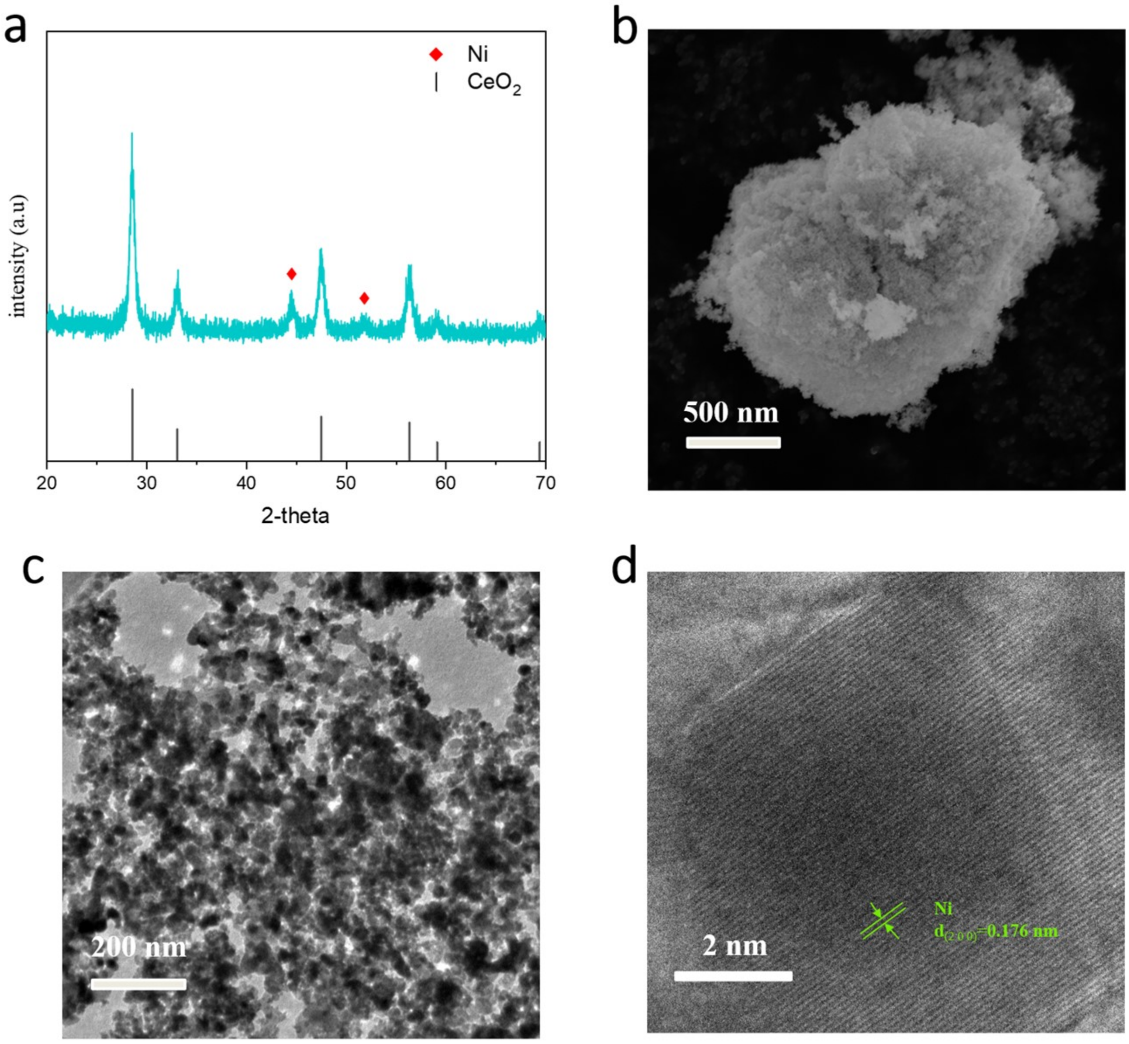

Fig. S7 The XRD pattern (a), SEM image (b), TEM image (c), high resolution TEM image (d), of Ni/CeO_2.

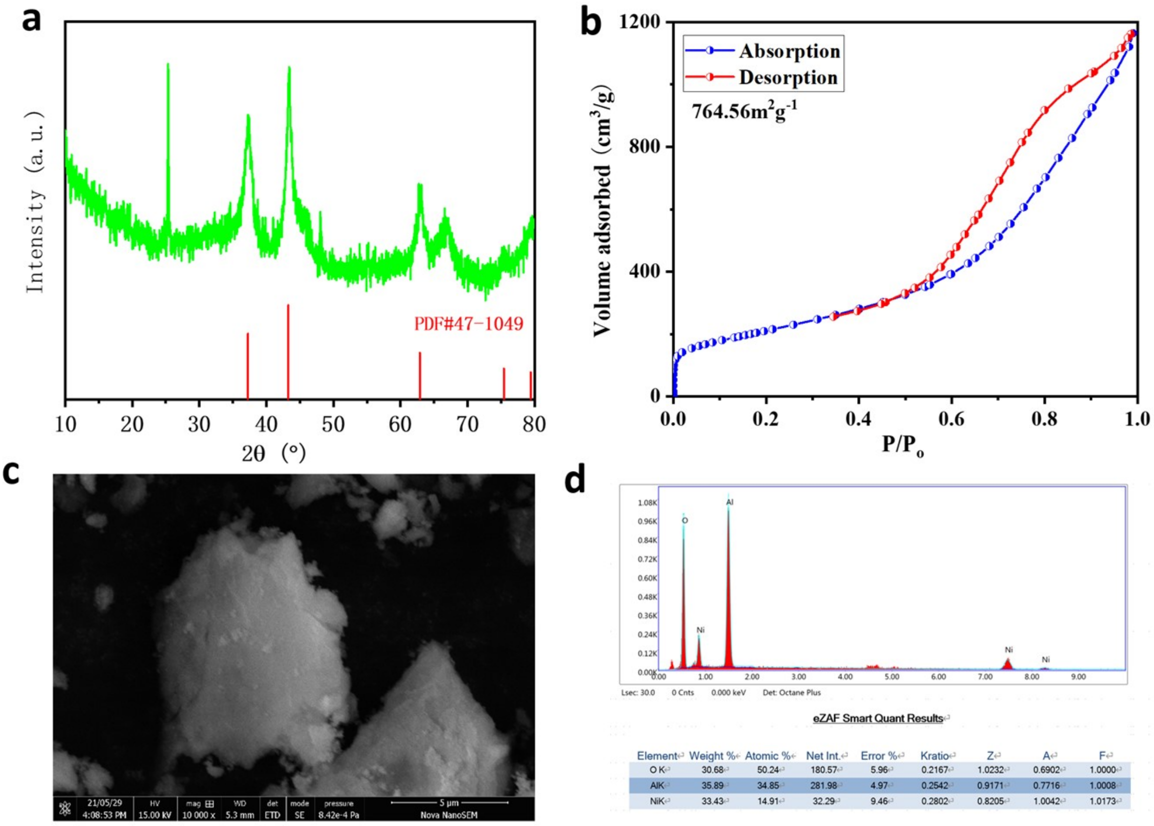

eZAF Smart Quant Results

Element	Weight %	Atomic %	Net Int.	Error %	Kratio	Z	A	F
O K	30.68	50.24	180.57	5.96	0.2167	1.0232	0.6902	1.0000
AlK	35.89	34.85	281.98	4.97	0.2542	0.9171	0.7716	1.0008
NiK	33.43	14.91	32.29	9.46	0.2802	0.8205	1.0042	1.0173

Fig. S8 (a, b, c, d) The XRD pattern, nitrogen adsorption and desorption isotherms, SEM image, EDS result of Ni/Al_2O_3 (SCST-241), which is purchased from SICHUAN SHUTAI CHEMICAL TECHNOLOGY CO.LTD.

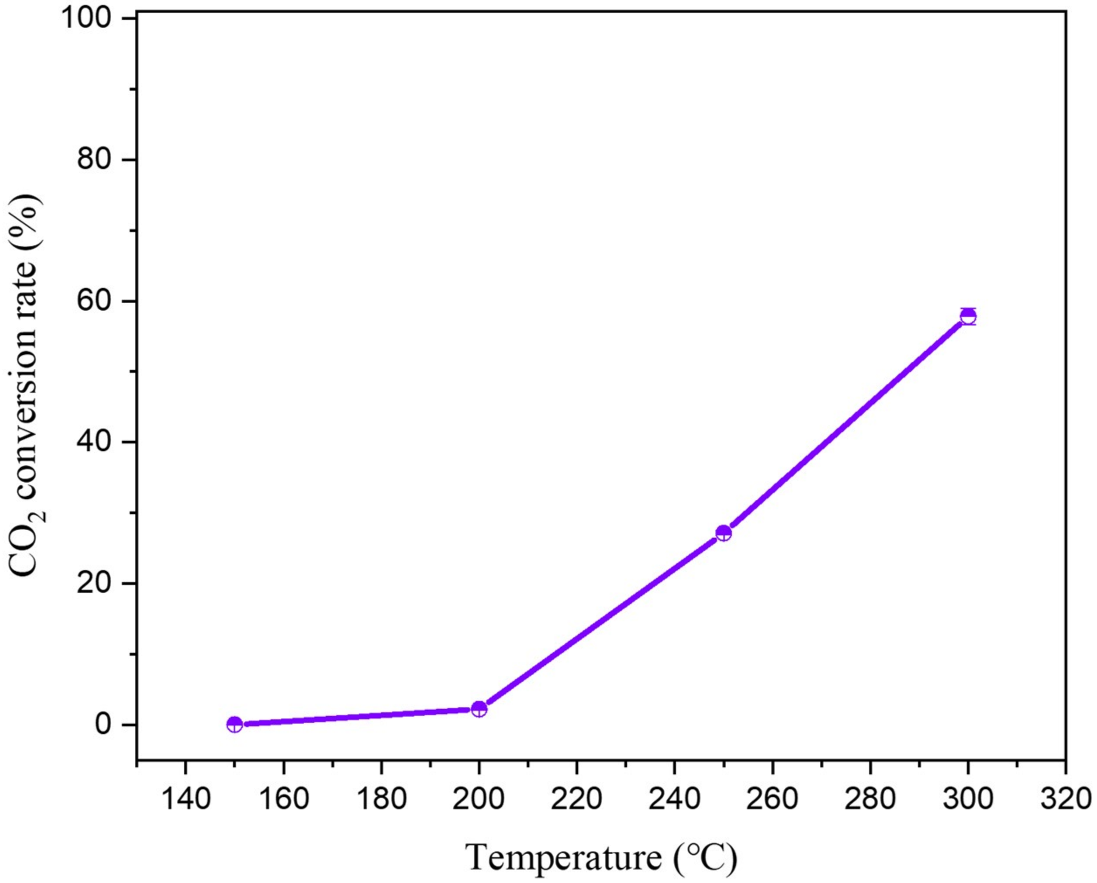

Fig. S9 The CO_2 conversion rate of thermocatalytic CO_2 methanation over 2D $Ni_1Ce_1O_3$. The CO_2 conversion rate = $(CH_4/CO_2)*100$, CH_4, CO_2 are the generation rate of CH_4, flow rate of CO_2, respectively.

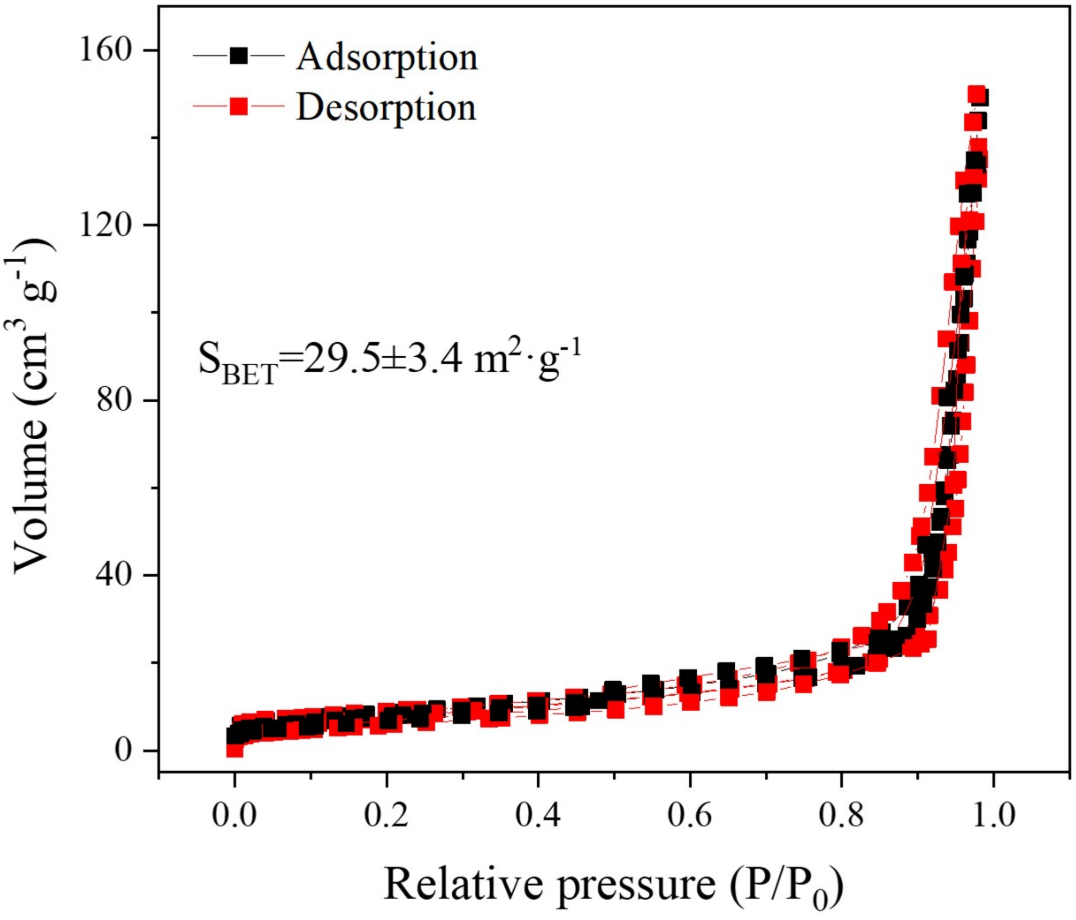

Fig. S10 The nitrogen adsorption and desorption isotherms of Ni/CeO_2.

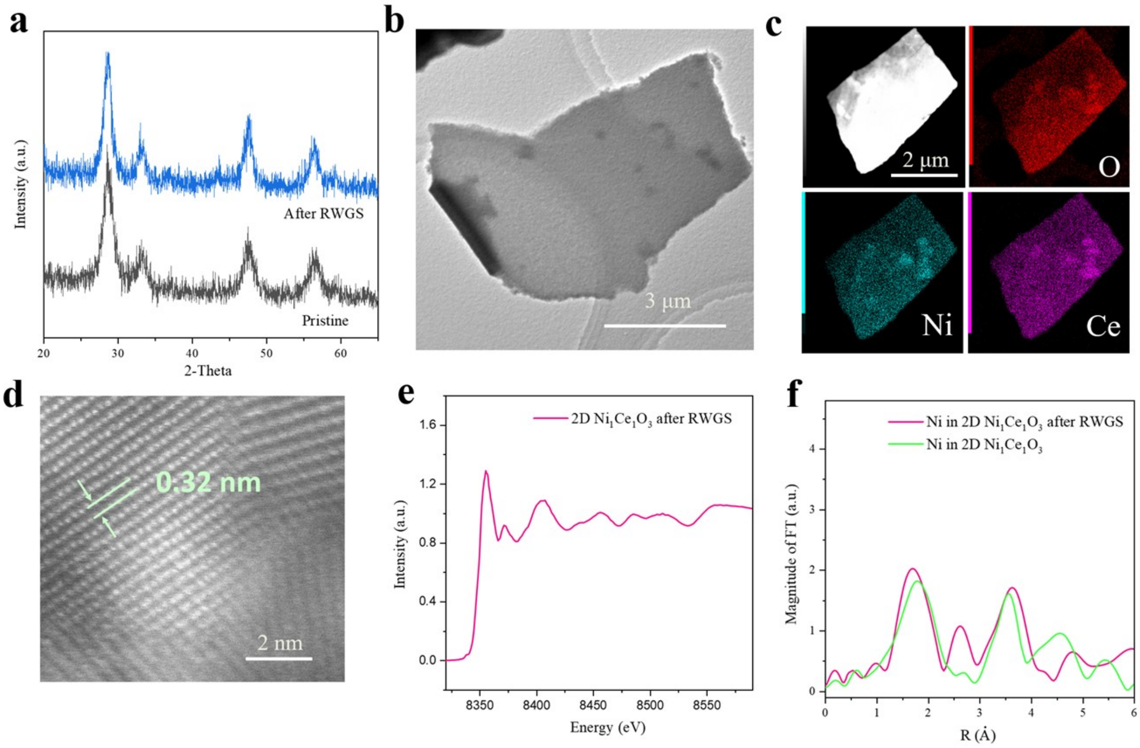

Fig. S11 The XRD pattern (a), TEM image (b), elemental mapping (c), HRTEM image (d) of 2D $Ni_1Ce_1O_3$ after long-term RWGS reaction. (e) The EXAFS of Ni K edge from 2D $Ni_1Ce_1O_3$ after long-term RWGS reaction. (f) FTEXAFS of Ni K edge from 2D $Ni_1Ce_1O_3$ before and after long-term RWGS reaction.

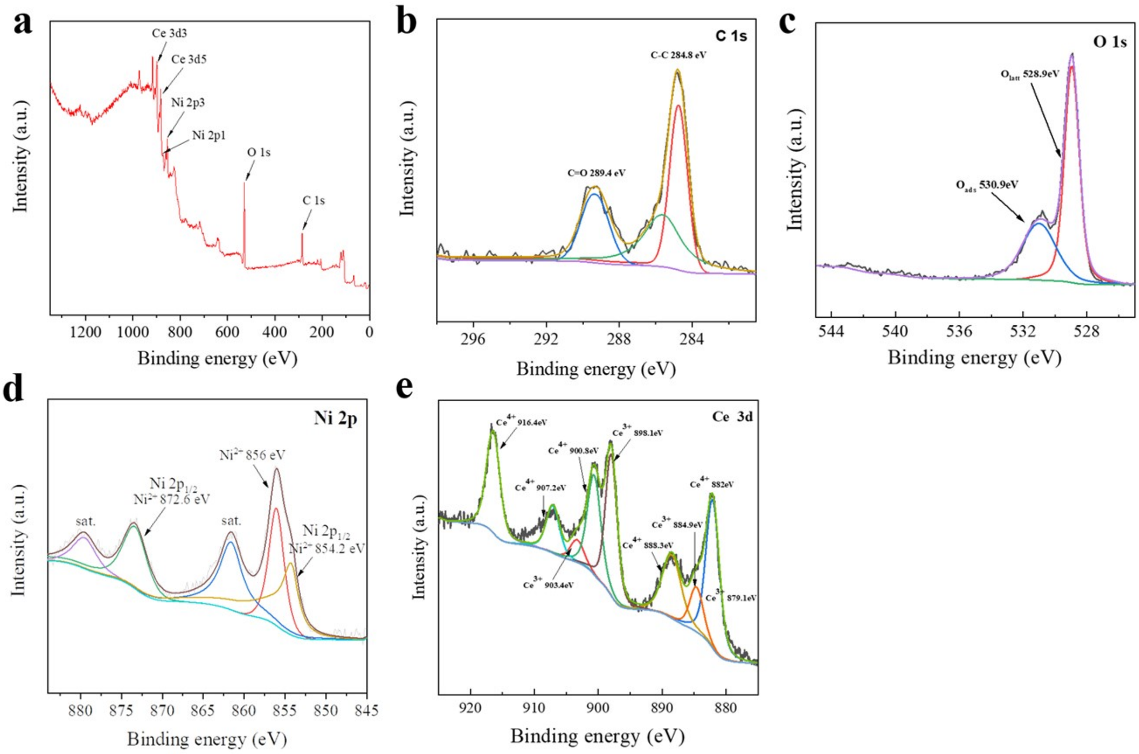

Fig. S12 The survey (a), C 1s spectrum (b), O 1s spectrum (c), Ni 2p spectrum (d), Ce 3d spectrum (e) of 2D $Ni_1Ce_1O_3$ after long-term RWGS reaction.

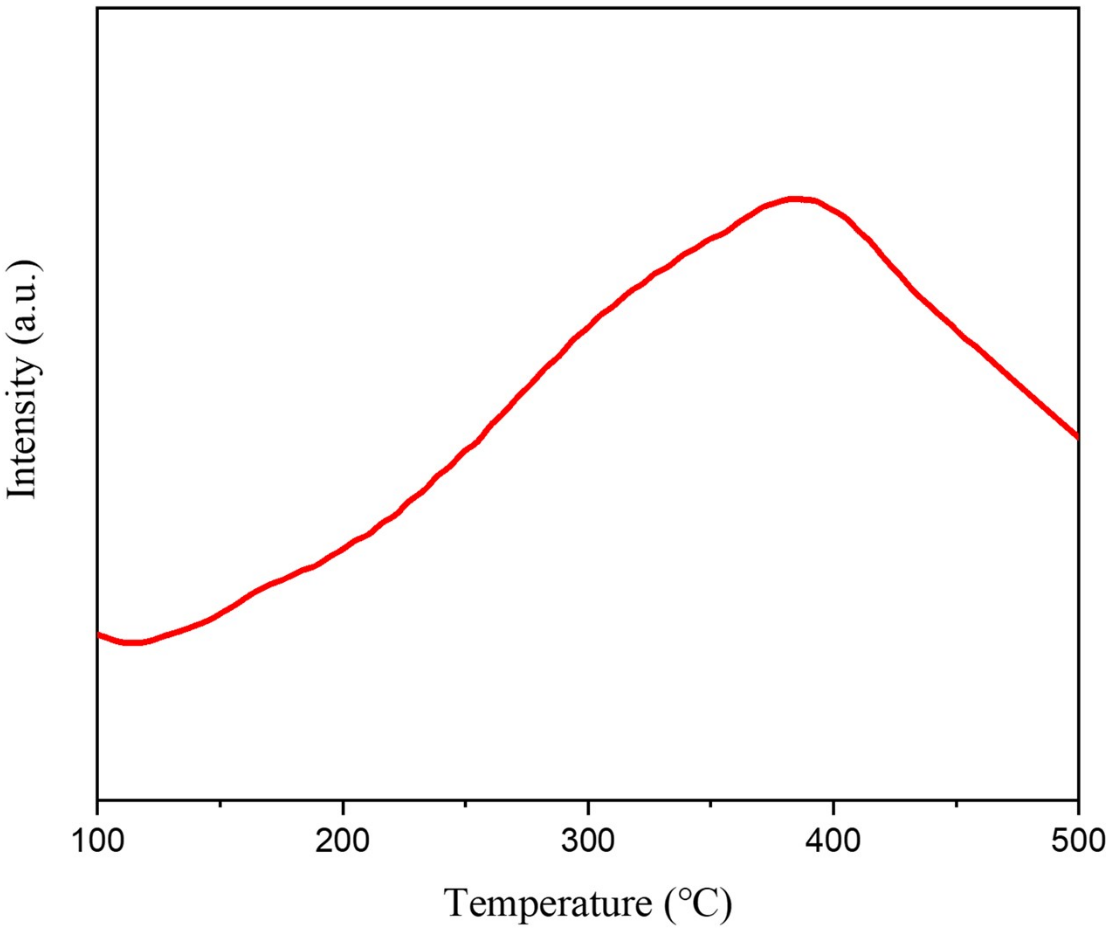

Fig. S13 CO_2-TPD curve of the 2D $Ni_1Ce_1O_3$.

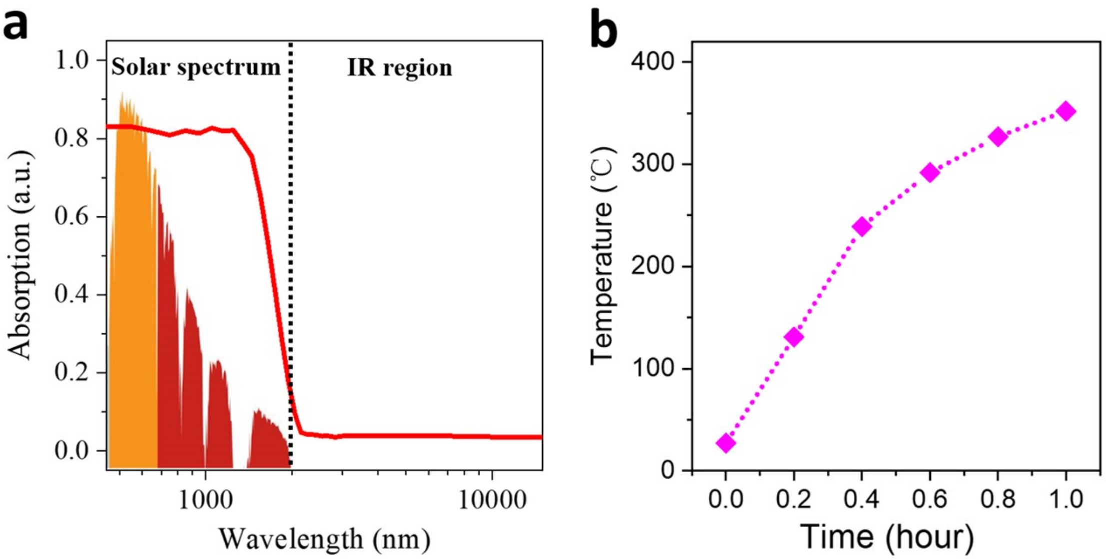

Fig. S14 (a) The normalized light absorption spectrum of TiC/Cu layer. (b) The temperature of catalyst loaded in TiC/Cu device, under 1 sun irradiation.

Fig. S14a shows that this TiC/Cu layer exhibits not only ~85% sunlight absorption in the wavelength of 0.4~1.8 μm but also nearly zero absorption in the IR wavelength region of 3-15 μm. Under 1 sun irradiation, the catalyst in TiC/Cu device can be heated to 352 °C in 1 hour (Fig. S14b).

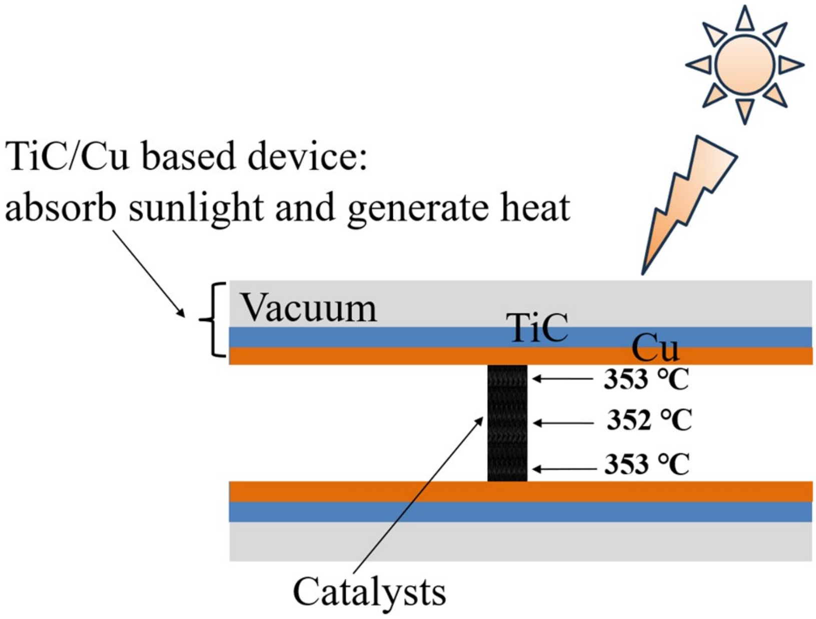

Fig. S15 The temperature distribution of catalysts loaded in TiC/Cu based device, under 1 sun irradiation.

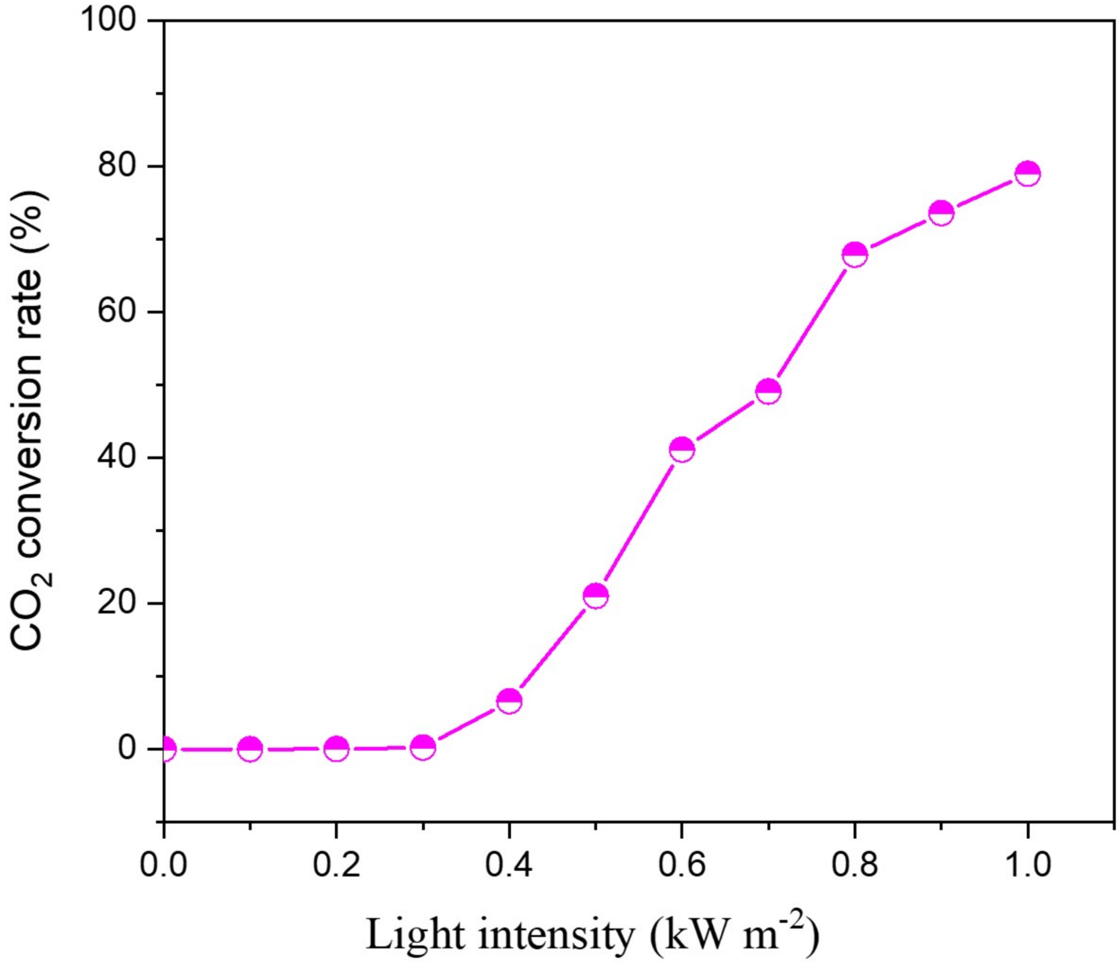

Fig. S16 The corresponding CO_2 conversion rate of photothermal CO_2 methanation over 2D $Ni_1Ce_1O_3$ in Fig. 4b. The CO_2 conversion rate = (CH_4/CO_2)*100, CH_4, CO_2 are the generation rate of CH_4, flow rate of CO_2, respectively.

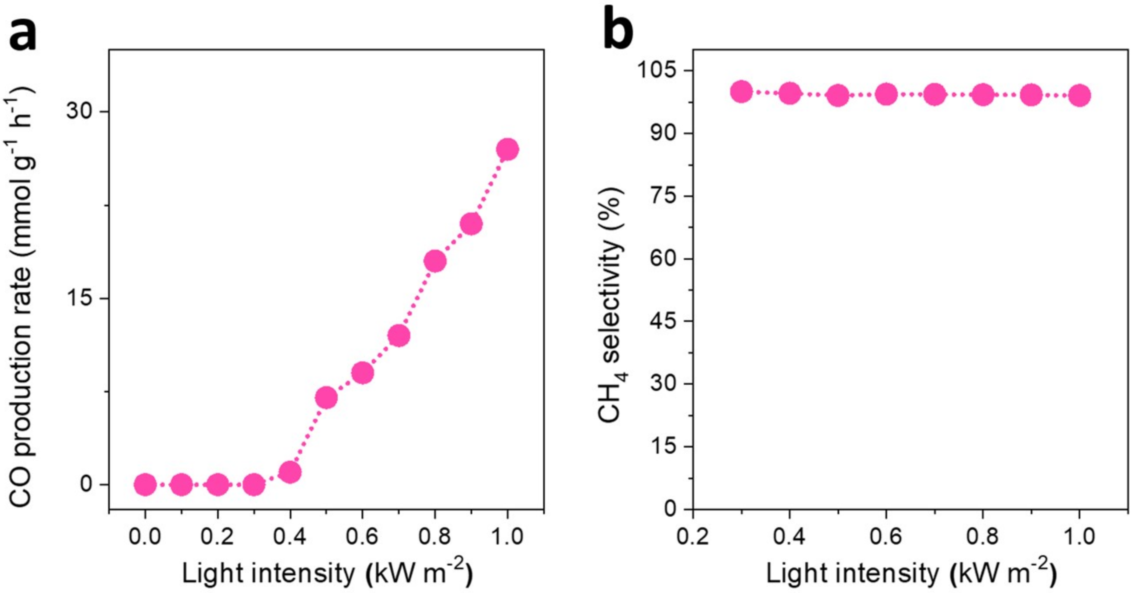

Fig. S17 (a) The CO production rate of photothermal CO_2 methanation over 2D $Ni_1Ce_1O_3$ loaded in TiC/Cu based device under different sunlight irradiation. (b) The corresponding CH_4 produced selectivity of photothermal CO_2 methanation over 2D $Ni_1Ce_1O_3$ loaded in TiC/Cu based device, in which the CH_4 selectivity = $CH_4/(CH_4+CO)$, CH_4, CO are the generation rate of CH_4, CO, respectively, from CO_2 methanation.

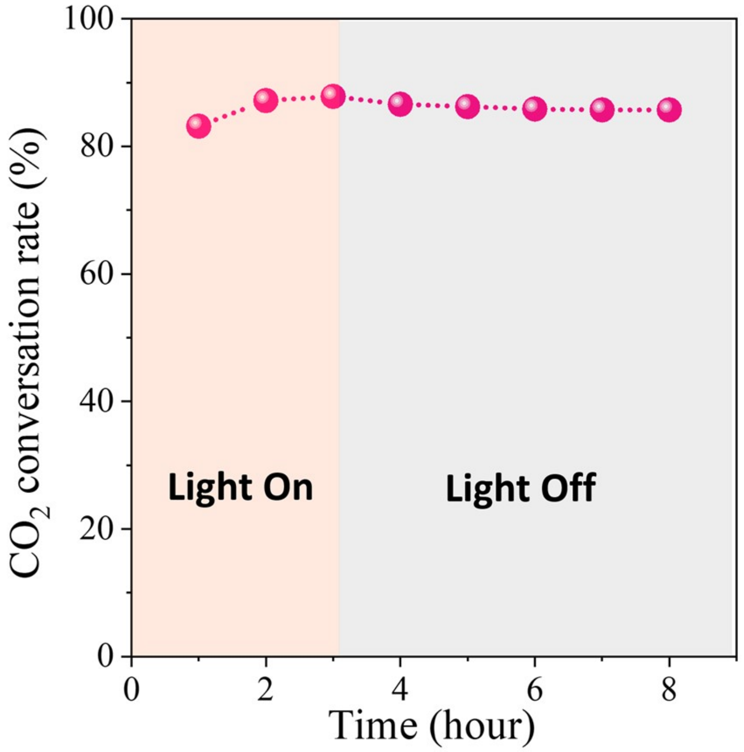

Fig. S18 The corresponding CO_2 conversion rate of photothermal CO_2 methanation over 2D $Ni_1Ce_1O_3$ in Fig. 4c. The CO_2 conversion rate = (CH_4/CO_2)*100, CH_4, CO_2 are the generation rate of CH_4, flow rate of CO_2, respectively.

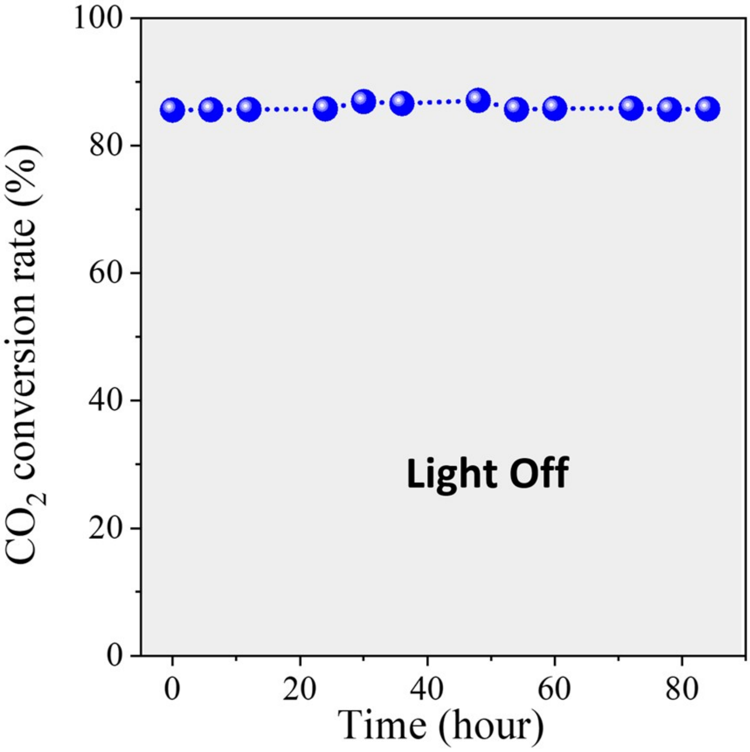

Fig. S19 The corresponding CO_2 conversion rate of photothermal CO_2 methanation over 2D $Ni_1Ce_1O_3$ in Fig. 4e. The CO_2 conversion rate = (CH_4/CO_2)*100, CH_4, CO_2 are the generation rate of CH_4, flow rate of CO_2, respectively.

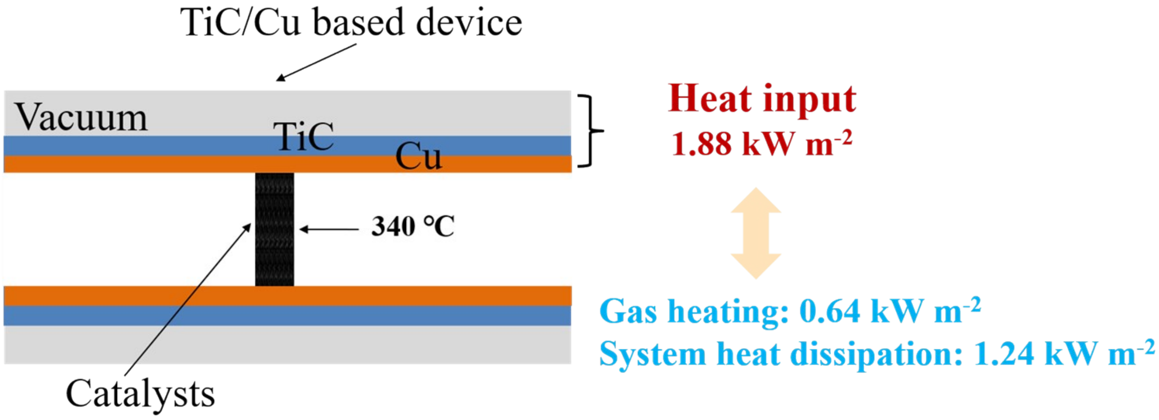

Fig. S20 The heat input and output diagram of self-operating photothermal methanation system without light irradiation.

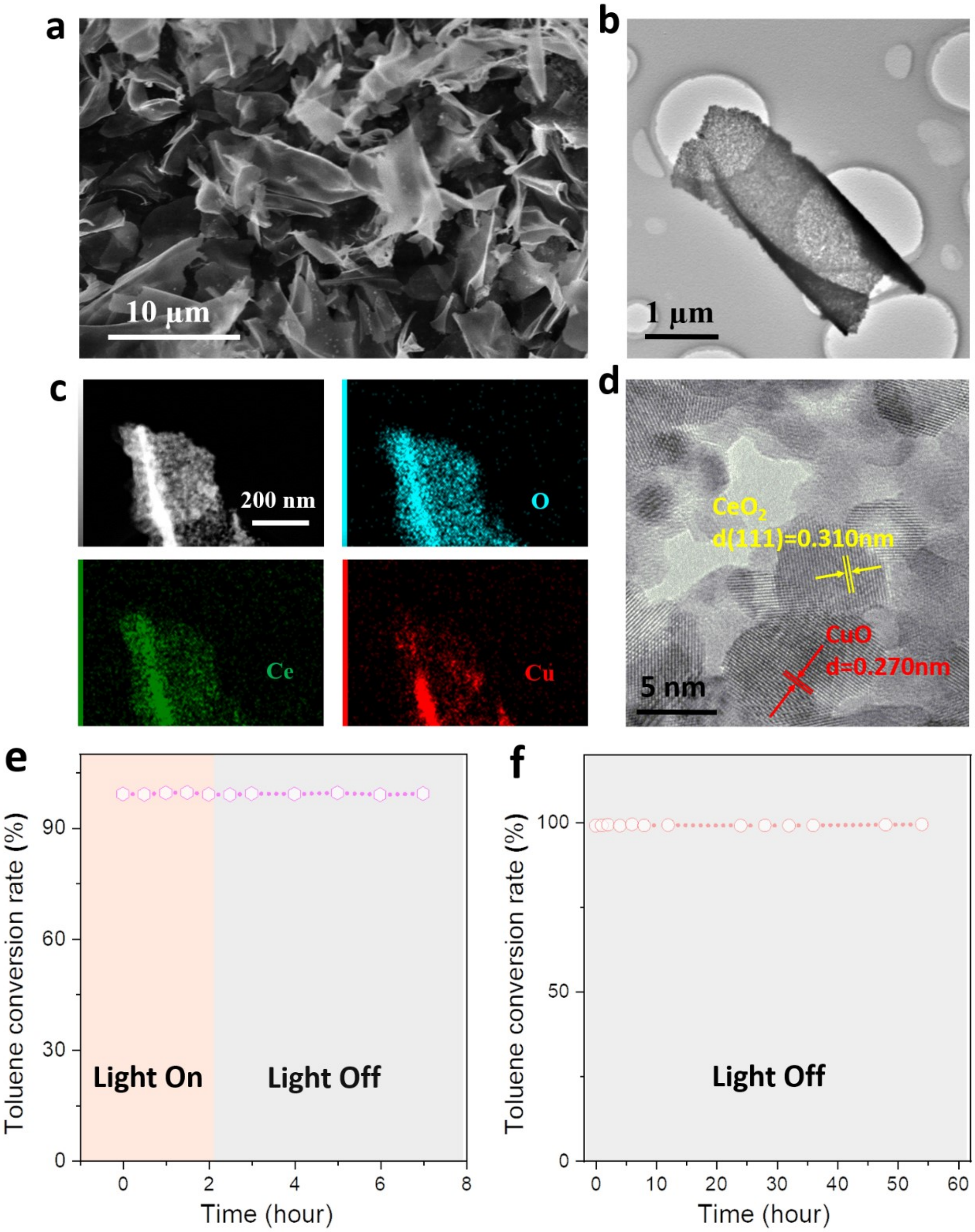

Fig. S21 (a) SEM image, (b) TEM image, (c) STEM image and elemental mapping, (d) HRTEM image of 2D CuO-CeO$_2$. (e) The toluene conversion rate of self-operating photothermal VOCs catalytic combustion system. (f) The toluene conversion rate of self-operating photothermal VOCs catalytic combustion system without light irradiation for 54 hours.

This system can also drive VOCs catalytic combustion by changing the 2D $Ni_1Ce_1O_3$ as a two-dimensional heterostructure of CuO and CeO_2 (2D CuO-CeO_2, Fig. S21 a-d). In the self-operating test, the toluene conversion rate of this system exceeds 99% under 2 hours of 1 Sun irradiation (Fig. S21 e). When the sunlight source is turned off, the system still maintains a toluene conversion rate of more than 99% in the followed 5 hours test. Fig. S21 f exhibits the stability of self-operating VOCs catalytic combustion system, and it is found that the system could maintain a toluene conversion of more than 99% in the 54 hours test.

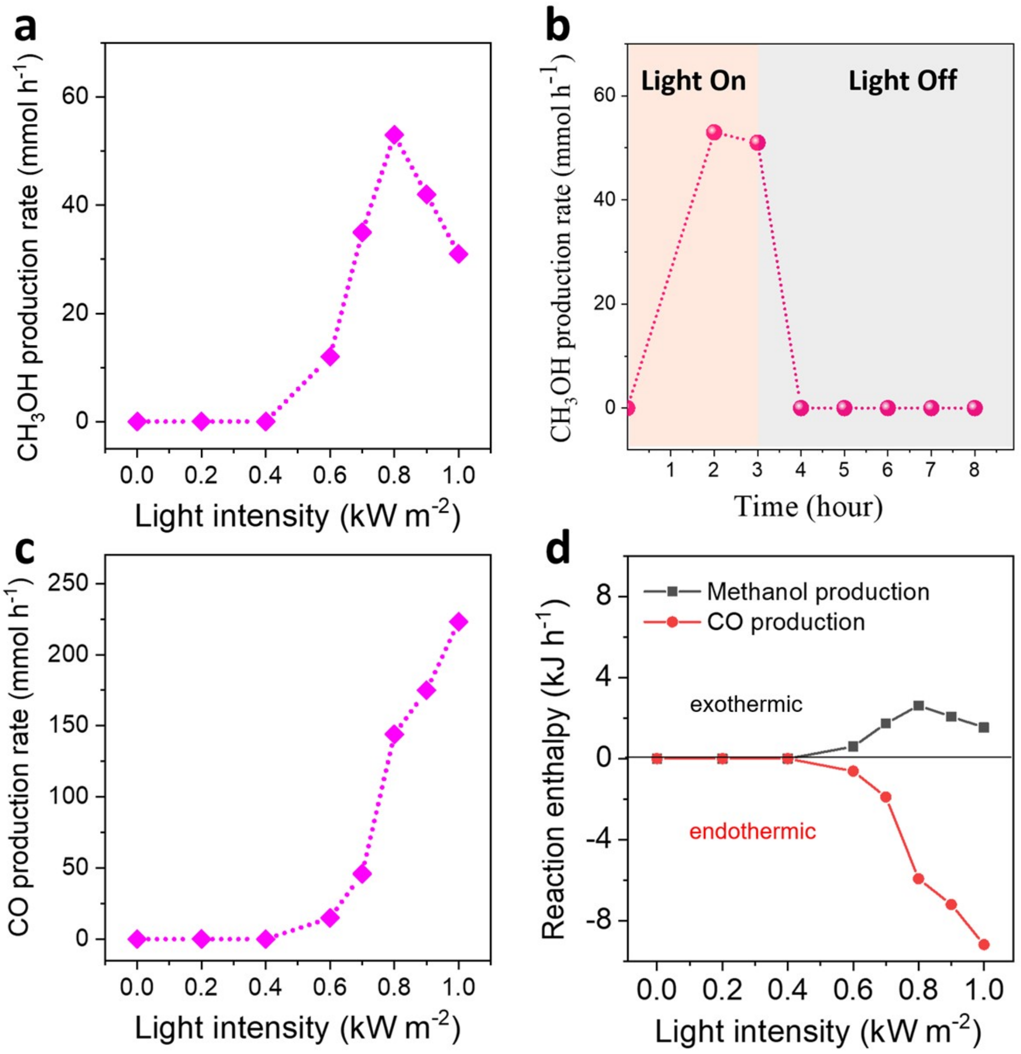

Fig. S22 (a) The methanol production rate of photothermal CO_2 hydrogenation over commercial CuZnAlO$_x$ loaded in TiC/Cu based device under different sunlight irradiation. (b) The methanol production rate of photothermal CO_2 hydrogenation over commercial CuZnAlO$_x$ loaded in TiC/Cu based device with and without 0.8 sun irradiation. (c) The CO generation rate of photothermal CO_2 methanation over commercial CuZnAlO$_x$ loaded in TiC/Cu based device under different sunlight irradiation. (d) The heat of methanol production and CO production from photothermal CO_2 hydrogenation under different sunlight irradiation. Positive values mean generate heat, negative values mean consume heat.

For the CO_2 hydrogenation to methanol (ΔH= -49.41 kJ mol^{-1}), 40 g of commercial CuZnAlO$_x$ (SCST-253, purchased from SICHUAN SHUTAI CHEMICAL TECHNOLOGY CO.LTD) is loaded in TiC/Cu based device and irradiated by light source (DL3000), the flow of feed gas is the mixture of 25 L h^{-1} of CO_2 and 75 L h^{-1} of H_2, which is operated at a pressure of 2.5 MPa to promote the generation of methanol. The reaction products are tested by gas chromatography (GC) 7890A equipped with FID and TCD detectors.

As shown in Fig. S22 a, under 0.6 kW m^{-2} intensity of sunlight (0.6 sun) irradiation, the photothermal CO_2 hydrogenation to methanol is clearly onset and achieves a peak methanol production value of 53 mmol h^{-1} under 0.8 sun irradiation. Afterwards, the production of methanol is stopped without sunlight irradiation, showing the unable of self-operation (Fig. S22 b). Besides producing methanol, we found that this system also produces by-product CO via reverse water-gas shift reaction (RWGS, $CO_2+H_2 \rightarrow CO+H_2O$, $\Delta H= 41.15$ kJ mol^{-1}), which is an endothermic reaction. Fig. S22 c shows that the RWGS CO production rates of system are 15, 46, 144, 175, 223 mmol h^{-1} respectively, under 0.6, 0.7, 0.8, 0.9 1 sun irradiation. Correspondingly, the heat consumptions are 0.61, 1.89, 5.92, 7.20, 9.18 kJ h^{-1}, higher than the heat energy generated by parallelled methanol production of 0.59, 1.73, 2.62, 2.07, 1.53 kJ h-1, respectively (Fig. S22 d). Therefore, the strong side reaction of RWGS makes the interruption of photothermal CO_2 hydrogenation to methanol without sunlight irradiation.

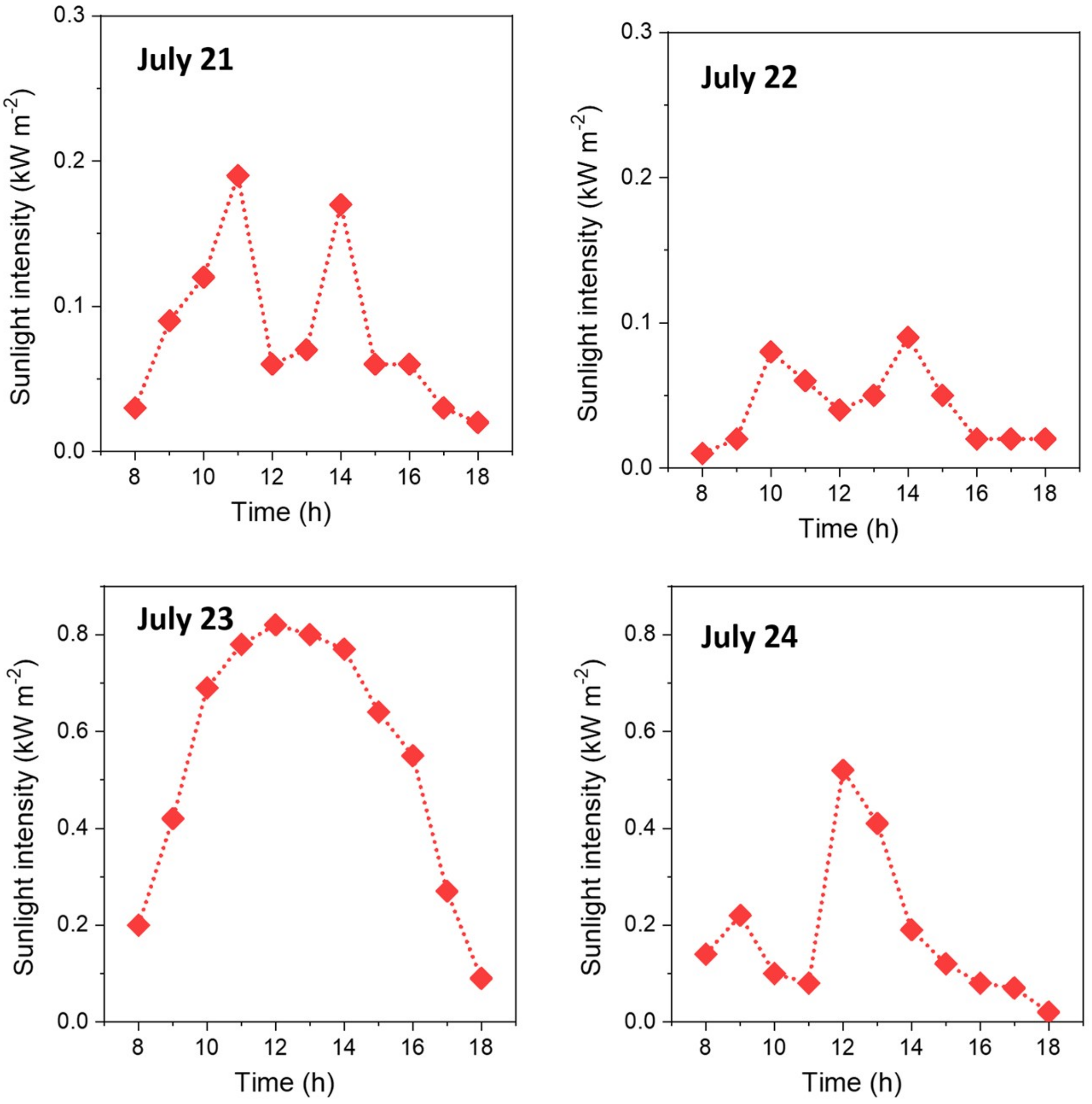

Fig. S23 The outdoor solar irradiation density change on July 21, 22, 23, 24, 2022, in the Baoding city, China.

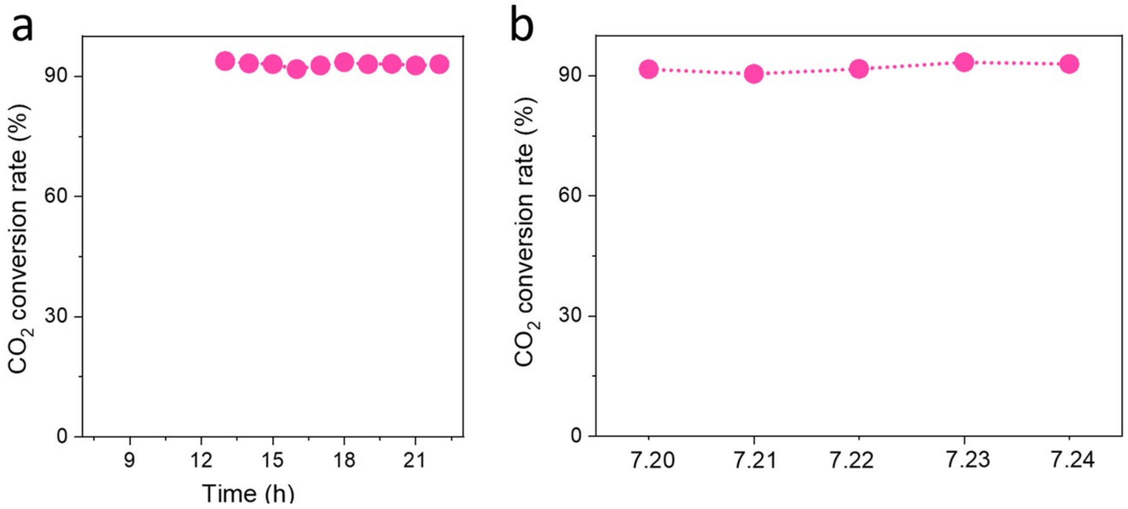

Fig. S24 (a) The corresponding CO_2 conversion rate of photothermal CO_2 methanation over 2D $Ni_1Ce_1O_3$ in Fig. 5c. (b) The corresponding CO_2 conversion rate of photothermal CO_2 methanation over 2D $Ni_1Ce_1O_3$ in Fig. 5d. The CO_2 conversion rate = (CH_4/CO_2)*100, CH_4, CO_2 are the generation rate of CH_4, flow rate of CO_2, respectively.

References

1. B. Ravel and M. Newville, *J. Synchrotron Radiat.*, 2005, **12**, 537-541.
2. G. Kresse and J. Furthmüller, *Comput. Mater. Sci.*, 1996, **6**, 15-50.
3. G. Kresse and J. Furthmüller, *Phys. Rev. B*, 1996, **54**, 11169-11186.
4. J. P. Perdew, K. Burke and M. Ernzerhof, *Phys. Rev. Lett.*, 1996, **77**, 3865-3868.
5. G. Kresse and D. Joubert, *Phys. Rev. B*, 1999, **59**, 1758-1775.
6. P. E. Blöchl, *Phys. Rev. B*, 1994, **50**, 17953-17979.
7. S. L. Dudarev, G. A. Botton, S. Y. Savrasov, C. J. Humphreys and A. P. Sutton, *Phys. Rev. B*, 1998, **57**, 1505-1509.
8. S. Grimme, J. Antony, S. Ehrlich and H. Krieg, *J. Chem. Phys.*, 2010, **132**, 154104.
9. C. Zhao, F. Li, Y. Yang, R. Lippi, H. Li and W. Chen, *Funct. Mater. Lett.*, 2020, **13**.
10. I. S. Khan, D. Mateo, G. Shterk, T. Shoinkhorova, D. Poloneeva, L. Garzón-Tovar and J. Gascon, *Angew. Chem., Int. Ed.*, 2021, **60**, 26476-26482.
11. J. A. H. Dreyer, P. Li, L. Zhang, G. K. Beh, R. Zhang, P. H. L. Sit and W. Y. Teoh, *Appl. Catal. B-Environ.*, 2017, **219**, 715-726.

12. T. Sakpal and L. Lefferts, *J. Catal.*, 2018, **367**, 171-180.
13. T. Zhang, W. Wang, F. Gu, W. Xu, J. Zhang, Z. Li, T. Zhu, G. Xu, Z. Zhong and F. Su, Appl. Catal. B-Environ., 2022, **312**, 121385.
14. M. Zhu, P. Tian, X. Cao, J. Chen, T. Pu, B. Shi, J. Xu, J. Moon, Z. Wu and Y.-F. Han, *Appl. Catal. B-Environ.*, 2021, **282**, 119561.
15. A. Quindimil, M. C. Bacariza, J. A. González-Marcos, C. Henriques and J. R. González-Velasco, *Appl. Catal. B-Environ.*, 2021, **296**.
16. Z. Zhao, Q. Jiang, Q. Wang, M. Wang, J. Zuo, H. Chen, Q. Kuang and Z. Xie, *ACS Sustainable Chem. Eng.*, 2021, **9**, 14288-14296.
17. A. Quindimil, U. De-La-Torre, B. Pereda-Ayo, A. Davó-Quiñonero, E. Bailón-García, D. Lozano-Castelló, J. A. González-Marcos, A. Bueno-López and J. R. González-Velasco, *Catal. Today*, 2020, **356**, 419-432.
18. S. Chai, Y. Men, J. Wang, S. Liu, Q. Song, W. An and G. Kolb, *J. CO_2 Util.*, 2019, **33**, 242-252.
19. X. Li, J. Lin, L. Li, Y. Huang, X. Pan, S. E. Collins, Y. Ren, Y. Su, L. Kang, X. Liu, Y. Zhou, H. Wang, A. Wang, B. Qiao, X. Wang and T. Zhang, *Angew. Chem., Int. Ed.*, 2020, **59**, 19983-19989.
20. S. López-Rodríguez, A. Davó-Quiñonero, E. Bailón-García, D. Lozano-Castelló and A. Bueno-López, *Mol. Catal.*, 2021, **515**, 111911.
21. R.-P. Ye, Q. Li, W. Gong, T. Wang, J. J. Razink, L. Lin, Y.-Y. Qin, Z. Zhou, H. Adidharma, J. Tang, A. G. Russell, M. Fan and Y.-G. Yao, *Appl. Catal. B-Environ.*, 2020, **268**.
22. X. Yu, X. Ding, Y. Yao, W. Gao, C. Wang, C. Wu, C. Wu, B. Wang, L. Wang and Z. Zou, *Adv. Mater.*, 2024, **36**, 2312942.
23. J. Zhou, Z. Gao, G. Xiang, T. Zhai, Z. Liu, W. Zhao, X. Liang and L. Wang, *Nat. Commun.*, 2022, **13**, 327.
24. S. Renda, A. Ricca and V. Palma, *Appl. Energy*, 2020, **279**, 115767.
25. Y. Guo, S. Mei, K. Yuan, D.-J. Wang, H.-C. Liu, C.-H. Yan and Y.-W. Zhang, *ACS Catal.*, 2018, **8**, 6203-6215.
26. S. Tada, O. J. Ochieng, R. Kikuchi, T. Haneda and H. Kameyama, *Int. J. Hydrogen Energy*, 2014, **39**, 10090-10100.
27. D. O. Kumi, T. N. Phaahlamohlaka, M. W. Dlamini, I. T. Mangezvo, S. D. Mhlanga, M. S. Scurrell and N. J. Coville, *Appl. Catal. B-Environ.*, 2018, **232**, 492-500.
28. H. Xin, L. Lin, R. Li, D. Li, T. Song, R. Mu, Q. Fu and X. Bao, *J. Am. Chem. Soc.*, 2022, **144**, 4874-4882.
29. X. Zhu, H. Zong, C. J. V. Pérez, H. Miao, W. Sun, Z. Yuan, S. Wang, G. Zeng, H. Xu, Z. Jiang and G. A. Ozin, *Angew. Chem., Int. Ed.*, 2023, **62**, e202218694.
30. J. Polanski, T. Siudyga, P. Bartczak, M. Kapkowski, W. Ambrozkiewicz, A. Nobis, R. Sitko, J. Klimontko, J. Szade and J. Lelątko, *Appl. Catal. B-Environ.*, 2017, **206**, 16-23.
31. H. Ge, Y. Kuwahara, K. Kusu, Z. Bian and H. Yamashita, *Appl. Catal. B-Environ.*, 2022, **317**, 121734.
32. L. Luo, M. Wang, Y. Cui, Z. Chen, J. Wu, Y. Cao, J. Luo, Y. Dai, W.-X. Li, J. Bao and J. Zeng, *Angew. Chem., Int. Ed.*, 2020, **59**, 14434-14442.
33. G. Fu, M. Jiang, J. Liu, K. Zhang, Y. Hu, Y. Xiong, A. Tao, Z. Tie and Z. Jin, *Nano Lett.*, 2021, **21**, 8824-8830.
34. Z. Li, R. Shi, J. Zhao and T. Zhang, *Nano Res.*, 2021, **14**, 4828-4832.
35. X. Liu, C. Xing, F. Yang, Z. Liu, Y. Wang, T. Dong, L. Zhao, H. Liu and W. Zhou, *Adv. Energy Mater.*, 2022, **12**, 2201009.

36. M. Cai, Z. Wu, Z. Li, L. Wang, W. Sun, A. A. Tountas, C. Li, S. Wang, K. Feng, A.-B. Xu, S. Tang, A. Tavasoli, M. Peng, W. Liu, A. S. Helmy, L. He, G. A. Ozin and X. Zhang, *Nat. Energy*, 2021, **6**, 807-814.
37. D. Mateo, N. Morlanes, P. Maity, G. Shterk, O. F. Mohammed and J. Gascon, *Adv. Funct. Mater.*, 2021, **31**, 2008244.
38. Y. Li, J. Hao, H. Song, F. Zhang, X. Bai, X. Meng, H. Zhang, S. Wang, Y. Hu and J. Ye, *Nat. Commun.*, 2019, **10**, 2359.
39. F. Sastre, A. V. Puga, L. Liu, A. Corma and H. García, *J. Am. Chem. Soc.*, 2014, **136**, 6798-6801.
40. Q. Li, Y. Gao, M. Zhang, H. Gao, J. Chen and H. Jia, *Appl. Catal. B-Environ.*, 2022, **303**, 120905.